

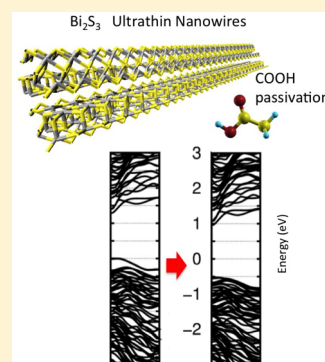
Atomistic Modeling of Morphology and Electronic Properties of Colloidal Ultrathin Bi₂S₃ Nanowires

Vasco Calzia,^{†,‡} Roberto Piras,[†] Andrea Ardu,[§] Anna Musinu,[§] Michele Saba,[†] Giovanni Bongiovanni,^{†,‡} and Alessandro Mattoni^{*,‡}

[†]Department of Physics, University of Cagliari, [‡]Istituto Officina dei Materiali, CNR-IOM SLACS Cagliari, and [§]Department of Chemical and Geological Sciences, University of Cagliari, Cittadella Universitaria, Monserrato, Cagliari I-09042, Italy

S Supporting Information

ABSTRACT: Ultrathin crystalline Bi₂S₃ nanostructures are studied by first-principles atomistic modeling and supported by experiments. Consistent with previous findings, the theoretical analysis shows that nanowires with lateral sizes as small as a few nanometers are energetically possible. Also, we were able to synthesize ultrathin nanowires by means of a low-cost, nontoxic colloidal route. Transmission electron microscopy data reveal a coherence length of the nanowires exceeding 30 nm. The simulations show that surfaces affect the electronic structure of the material inducing peculiar 1D-like electronic states on the nanowire edges that are located 300 meV above the valence band. Sulfur vacancies are instead responsible for localized states a few hundred millielectronvolts below the conduction band. The possibility of eliminating the surface-induced intragap states is theoretically investigated by passivating the surfaces of the nanowires with carboxylic and amine groups that are commonly employed in colloidal synthesis. Small molecules methylamine and acetic acid are expected to fully passivate the surfaces of the nanowires, removing the edge states and restoring a clean band gap. Present results suggest a possible route for improving optoelectronic properties of Bi₂S₃ nanostructures by tuning the size of the ligand molecules.



INTRODUCTION

Semiconductor nanocrystals are exploited in several fields of science and engineering, including light-emitting diodes,^{1–3} photodetectors,^{4,5} solar cells,^{6–8} field effect transistors,^{9,10} and many others. Nanocrystals can be synthesized by a variety of techniques (such as chemical bath deposition¹¹ and solvothermal¹² and colloidal methods¹³) that make possible accurate control over their size and shape and, in turn, their optoelectronic properties through quantum confinement phenomena. Among nanocrystals, Bi₂S₃ is an important material for optoelectronics because of its high optical absorption coefficient (10⁴ cm⁻¹)¹⁴ as well as its small band gap (reported in literature between 1.3 and 1.6 eV^{15–21}) that make it ideal in photodetector devices²² and as sensitizer or electron acceptor in photovoltaics.^{23–27} A distinctive feature of this material is its biocompatibility^{28,29} that allows the use of Bi₂S₃ for environmentally friendly devices or in biomedicine.³⁰ Colloidal Bi₂S₃ nanocrystals have been synthesized in several shapes, including dots,^{24,31,32} nanorods,^{31,33–38} nanowires,^{35,39–42} flowers,^{35,37,43,44} and nanotubes.¹⁴ Similar to other pnictogen chalcogenides, the crystalline structure of Bi₂S₃ exists in the periodic aggregation of ribbons, a feature that enables the synthesis of elongated nanostructures. Nanowires (NWs) ensure high surface-to-volume ratio, an important requirement for catalytic applications.

Monocrystalline Bi₂S₃ NWs reported so far in literature exhibit a minimum diameter of the order of tens of nanometers. Thinner structures were studied by Cademartiri et al.,^{39,40} who

synthesized polycrystalline NWs with diameter as small as 1.6 nm. However, the coherence length of such nanostructures was very short (~2 nm). Ultrathin NWs with greater coherence length are desirable for improving electronic conductivity. The morphology of Bi₂S₃ nanostructures also plays an important role on the optical properties. There is no experimental evidence of photoluminescence (PL) from Bi₂S₃ nanocrystals obtained by colloidal synthesis. Light emission has been observed in some studies^{34,37,45,46} based on hydrothermal synthesis of Bi₂S₃ nanocrystals but at energies that are much higher than the optical gap of the material, even taking into account quantum confinement effects.³¹ The absence of PL in colloidal synthesis has been explained by assuming an high concentration of trap states in the nanocrystals, possibly caused by the presence of abundant sulfur vacancies.⁴⁷ Such defect states are particularly undesired in photovoltaic devices because they inhibit carrier transport and promote charge recombination. A possible source of traps could also be the surface of the nanocrystals because of its incomplete passivation by organic ligands. Surface passivation is typically obtained by oleic acid^{22,31,48} and oleylamine,^{36,39} two surfactants that bind to the nanocrystals with their polar head and expose their apolar alkyl tail toward the solvent. Previous experiments⁴⁹ show that full coverage of the NWs by means of oleylamine is possible.

Received: March 20, 2015

Revised: June 29, 2015

Published: June 29, 2015

However, the persistence of poor optical properties suggests that either a fraction of surface sites remains unpassivated or that they interact with atoms that do not remove the dangling bonds (e.g., the aliphatic tails of the surfactant). The nature of the traps and the ability of organic ligands to passivate them is an important topic. Another relevant issue related to the surface is the effect of strain on electronic properties. This is particularly important for ultrathin nanowires having a very high surface-to-volume ratio. The control of the electronic energy levels of NWs is important to enable the extraction of photogenerated carriers in optoelectronic devices.⁵⁰ Accordingly, there is a need of fundamental understanding of ultrathin NWs structure and surfaces of the associated electronic levels and the mechanism of passivation.

In the present work, we study ultrathin NWs grown along the [010] crystallographic direction. By first-principles calculations, we show that ultrathin NWs are stable against separation into isolated ribbons and that the stability increases with diameter d . For NWs with $d < 2$ nm, the cohesion of the NW is small yet sufficient to have stable NWs at room temperature, as reported in ref 49. Larger ultrathin crystalline NWs (Figure 1) are obtained in the present work by a novel oleylamine-based organometallic synthesis employing bismuth acetate as precursor.

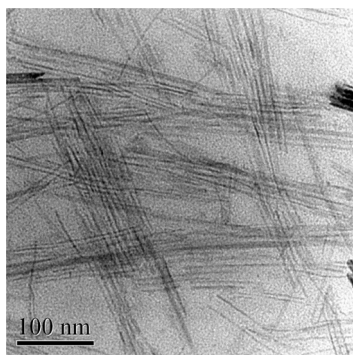


Figure 1. TEM image of Bi_2S_3 nanowires, obtained by oleylamine-based colloidal synthesis.

The electronic properties of the ultrathin Bi_2S_3 nanowires are further investigated within the framework of density functional theory (DFT). We find that intragap states of Bi_2S_3 nanowires (acting as nonradiative recombination centers) are likely due to the presence of point defects (such as sulfur vacancies) and free surfaces. In particular, we identify the sites of the NW surfaces that are responsible for the electronic levels within the gap. The calculations show that NWs with a clean electronic band gap can be obtained through selective organic passivation of the edges by short carboxylic or amines molecules. In agreement with previous experimental reports,⁴⁹ this result suggests a possible route for improving the optoelectronic properties of Bi_2S_3 nanostructures by tuning the ligand size.

RESULTS

Energetics of the Nanowires. The thermodynamic stability of nanoparticles is determined by their total configurational energy; the most stable atomic configurations are those with the lowest energy values. For thin nanowires formed by a small number of ribbons, it is possible to calculate their energy from first-principles. We consider NWs (Figure 2a) of increasing diameter built of 1, 4, 7, and 9 ribbons, respectively

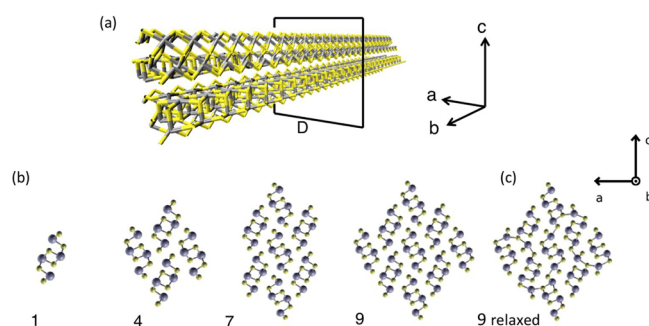


Figure 2. (a) Perspective view of an atomistic model of Bi_2S_3 NW extending along the b direction. (b) Cross-sectional view of NWs composed by 1, 4, 7, and 9 ribbons. (c) Comparison between a NW before (left) and after (right) energy minimization.

(Figure 2b). In particular, the largest 9-ribbon model has a diameter as large as 3 nm. All the NWs are periodic along the ribbon axis and are obtained by cutting the corresponding number of ribbons from a perfect bulk followed by the full relaxation of atomic structure through conjugate-gradient minimization.

Cohesive energy per atom ΔE of the nanowires is defined as

$$\Delta E = \frac{E - rE_{\text{rib}}}{N} \quad (1)$$

where E is the total energy of the NW formed by r ribbons and N atoms and E_{rib} is the total energy of the single isolated ribbon. A negative value of ΔE means that the wire is stable against its separation into isolated ribbons: the lower the ΔE value, the higher the stability and the cohesion between ribbons.

The results for ΔE are reported in Figure 3. The cohesive energy of the single ribbon is zero by definition. For larger

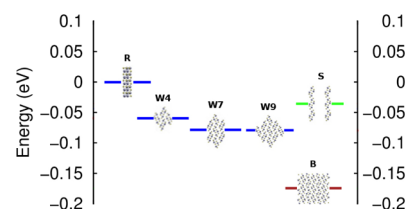


Figure 3. Energy difference per atom, ΔE , of the Bi_2S_3 nanostructures. The nanowires (W4, W7, and W9) get more stable with respect to the single ribbon (R) by increasing their diameter. Also, the cases of lamellar structure along the c direction (S) and the bulk (B) are reported for comparison.

diameter NWs, ΔE decreases monotonically, i.e., the structures become more stable. The bulk is found at $\Delta E = 0.18$ eV/atom, and it represents the lowest value attainable in the limit of NWs with infinite diameters. The analysis shows that the NWs are stable against dissociation into isolated ribbons. For NWs formed by 4 ribbons, the energy cost to dissociate the NW is small (about 60 meV/atom) but enough to have stable NWs at room temperature. This result is consistent with ref 40, reporting ultrathin nanowires formed by 4 ribbons. The NWs formed by 7 or more ribbons have an energy gain of about 80 meV/atom with respect to the single ribbon. By comparing the energy of the NWs with respect to the bulk, we can estimate a moderate excess energy associated with the large surface-to-volume ratio of about 0.1 eV/atom. The fact that the cohesive

energy per atom increases with the diameter can be explained in terms of the cost associated with the surfaces, which scales as $\sim 1/R$. We point out that this analysis compares NWs performed in vacuo with different sizes and does not estimate the activation energy requested to increase the diameter. The activation energy depends on the actual microscopic growth mechanism and on the specific nonequilibrium conditions. Depending on the experimental environment (solvents, ligands, thermodynamic parameters, etc.), large activation energy barriers for growth are possible. This could explain the inherent stability for the 4-ribbon structures reported in ref 40.

For completeness, we also considered the case of ultrathin Bi_2S_3 lamellar structures (Figure 3, S) formed by a regular array of parallel ribbons. In particular, we calculated the energy of the *c*-oriented lamellar structure that as it will be shown later provides the preferential inter-ribbon electronic coupling and the largest energetic stability. The calculated energy suggests that though possible lamellae are higher in energy than cylindrical NWs. We expect that the former will spontaneously fold into NWs by an exothermic relaxation.

Although NWs are higher in energy than the bulk, they do not undergo phase transformations or amorphization during the relaxation of atomic forces. During the relaxation of the NWs (Figure 2c), the sulfur atoms of the surfaces tend to move inward in order to compensate for the reduced atomic coordination with respect to the bulk, generating a strain on the surfaces. This effect is related to the presence of free surfaces, and it is likely reduced in the case of a full organic coverage.⁴⁹ Apart from the above strain effects, the unpassivated NWs in vacuo are stable and preserve their overall crystallinity.

The theoretical results show that crystalline Bi_2S_3 ultrathin NWs grown along the [010] crystallographic direction are in principle stable. In this work, we are able to synthesize crystalline nanostructures with diameters down to ~ 3 – 4 nm by performing an oleylamine-based organometallic synthesis (Methods). The colloidal dispersion in toluene was very stable. Figure 4 reports the high-resolution transmission electron

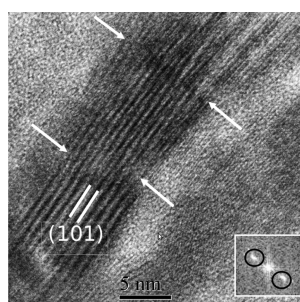


Figure 4. HR-TEM image of a portion of Bi_2S_3 nanowire, where nanocrystals are iso-oriented along the [010] direction; grain boundaries are present between the nanocrystals (arrows).

microscopy (HR-TEM) image of Bi_2S_3 -NW samples. Despite the unavoidable blurring (because of the coating with the insulating long molecules of surfactant), the TEM images show the morphological and structural features of the nanowires. X-ray diffraction pattern data indicates the presence of orthorhombic bismuthinite as a single crystalline phase (Supporting Information). NWs with lengths exceeding 300 nm were obtained.

The HR-TEM data shows that the coherence length of the NWs is around 30 nm (Figure 4). It also highlights that the (101) planes are perpendicular to the NWs axis, i.e., the wires grow along the [010] direction. Imperfections similar to grain boundaries can be attributed to the growth mechanism of the NWs, which exist in the consecutive nucleation of nanocrystals on the elongated structure. However, each nanocrystal preserves the crystallographic orientation of the wire. The boundaries can be better explained as a small variation of the NW diameter, whereas the core crystalline structure is common to all the nanocrystals. The preferential orientation of the NWs makes them linear in contrast with the case of Bi_2S_3 ultrathin NWs reported so far in literature that are flexible and do not exhibit a long-range crystallographic order.

Electronic Properties of Bulk and Inter-Ribbon Coupling. To understand the electronic properties of NWs in view of possible technological applications, we perform a comprehensive atomistic study based on first-principles electronic methods. The starting point is a detailed analysis of the inter-ribbon interactions within the crystalline bulk. As discussed above, the cohesion between Bi_2S_3 ribbons ranges from ~ 0.1 eV per atom for ultrathin NWs up to ~ 0.2 eV per atom for the bulk. This cohesive energy is large enough to keep ribbons aggregated within the crystal but it is one order of magnitude smaller with respect to intra-ribbon covalent forces (>1 eV per atom). Accordingly, the electronic coupling between ribbons is small, though important for the electronic properties of NWs and their surfaces. Important information about inter-ribbon coupling can be obtained from the analysis of the band structure of the bulk Bi_2S_3 and the effective electron mass (Figure 5a). By focusing on the conduction bands (CBs), we observe a large dispersion along the directions of the reciprocal space that are parallel to the ribbon axis, i.e., Γ -Y, S-X, and U-R, in agreement with previous theoretical literature.⁵¹ (Note the different *Pbnm* notation.) This is consistent with a high electron mobility along the ribbon.

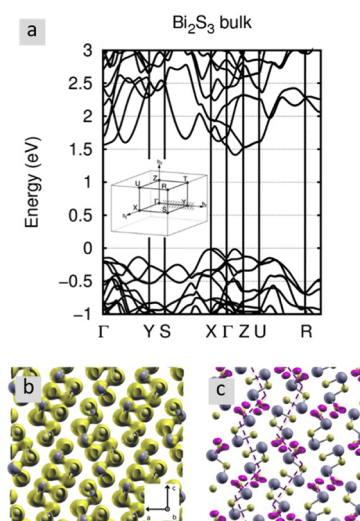


Figure 5. (a) Electronic band structure of Bi_2S_3 crystalline bulk. The band gap (located within Γ -Z) is direct and equal to 1.4 eV. The energy is set to zero at the valence band maximum. Inset shows the high symmetry directions in the reciprocal space of the crystal. (b) Representation of the 0.04 e Bohr^{-3} charge density isosurface of the Bi_2S_3 . (c) Charge density difference (CDD) between the bulk and the isolated ribbons corresponding the value $0.003 \text{ e Bohr}^{-3}$.

Concerning the effective mass of electrons, we first observe that the minimum of the CBs is placed between the Γ and Z points, where a direct transition corresponding to an electronic gap of 1.4 eV is calculated. The effective masses of the electrons in Bi_2S_3 (normalized to free electron mass) are calculated at the CBs minimum along the three Cartesian directions, and they are $m_a^*/m_e = 3.4$, $m_b^*/m_e = 0.8$, $m_c^*/m_e = 2.1$. These data confirm a higher mobility and a larger electronic coupling of the electrons along the ribbon axis. Concerning the inter-ribbon interaction in the a - c plane, the lower value of m_c^* with respect to m_a^* suggests a preferential coupling along the c direction.

The above anisotropy is explained by analyzing the charge density (CD) of the system (Figure 5b). For isosurfaces up to $4 \times 10^{-2} e \text{ Bohr}^{-3}$, there is no overlap between the electronic clouds of the single ribbons. Only at much lower values is a linking between the density of the ribbons observed. We can better visualize it by plotting the charge density difference (CDD) between the bulk and the isolated ribbons, calculated as $\text{CDD} = \text{CD}_{\text{bulk}} - \text{CD}_{\text{isolatedribb}}$. In Figure 5c, the CDD isosurface is reported, corresponding to the isovalue $3 \times 10^{-3} e \text{ Bohr}^{-3}$. It can be observed the presence of charge lobes between the outer Bi and S atoms of neighboring ribbons that give rise to stripes (dashed lines) of weakly interacting ribbons along the c direction. Similar electronic coupling is not observed in the a direction, and this is consistent with the inequality $m_c^* < m_a^*$.

Present analysis of the bulk electron density confirms that to a first level of approximation Bi_2S_3 behaves as a quasi-1D semiconductor whose electronic properties can roughly be described by the single-ribbon model.¹⁵ In contrast, a small inter-ribbon coupling takes place particularly along the c crystallographic direction that must be taken into account when considering NWs and their surfaces.

Electronic Properties of the Nanowires. In Figure 6, we report the electronic density of state (DOS) of the crystalline bulk (Figure 6a) and of the 4-ribbon NW (Figure 6b). Occupied states are represented by filled curves. We identify two main features of the nanowire DOS that are not present in the bulk: (1) a peak at 300 meV above the valence band corresponding to the highest occupied level of the NW, and (2) an increase of the density of states close to the top of the valence band. The two features are observed in all the NWs investigated. We first discuss point 1. By analyzing the atomic projections of the electronic wave function, it is found that the highest occupied states are p -type orbitals localized on the outer edge sulfurs of the NWs (magenta lobes in Figure 6, right). Interestingly, the DOS involves mainly two lines of sulfur atoms at the opposite edges of the NWs instead of being distributed over all external sulfur atoms. These states are doubly degenerate because there are two sulfur atoms within each unit cell that are equivalent by symmetry.

To better characterize the nature of the states, we analyze the band structure of the NW (Figure 7a). It is found that along the Γ -Y direction the two degenerate defect lines located above the continuum valence band are not flat but rather are dispersed in energy following the shape of the valence band. We conclude that the defect states are delocalized along the ribbon (b direction). The above analysis shows that the peak 1 can be attributed to the edges of the ribbon that induce electronic states localized within the plane perpendicular to the ribbon (a - c plane) but delocalized along the ribbon b direction. We conclude that the peculiar crystalline structure of Bi_2S_3 NWs formed by weakly interacting ribbons results in 1D-like surface states at the NWs edges. Interestingly, the

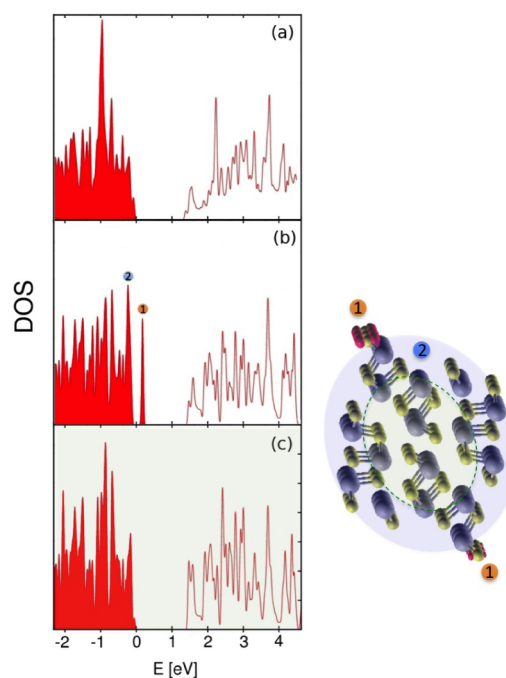


Figure 6. DOS of (a) the Bi_2S_3 bulk and (b) the 4-ribbon nanowire. (c) Nanowire DOS projected on its core atoms (see text). Right: Representation of the core (green) and surface (blue) of the NW; the valence top orbital localized on the sulfurs atoms at the nanowire edges are also shown (magenta color).

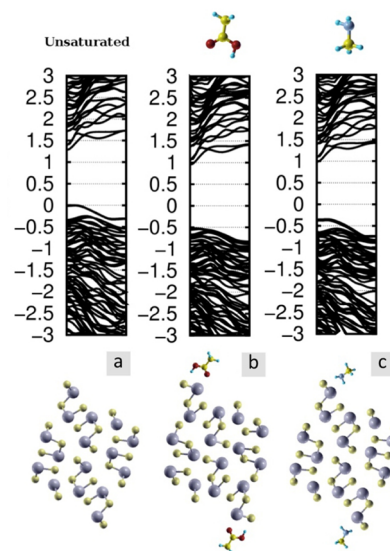


Figure 7. Band structure of the 4-ribbon nanowire (a) before and after saturation with (b) acetic acid and (c) methylamine. Acetic acid appears to be more efficient in lowering the surface band below the valence band. Minimum energy configurations of 4-ribbon nanowire decorated by acetic acid (top) and methylamine molecule (bottom).

energy position of this level (0.3 eV above the valence band) is compatible with the results of spectroscopic measurements in Bi_2S_3 .³¹

The surface of the NW is also responsible for the DOS peak 2. In contrast with the previous case, these levels are not localized on a specific atom and can be attributed to the strain of the surfaces (represented by the blue region in the atomistic model of Figure 6, right). To validate this hypothesis, we

calculate the core-projected DOS (Figure 6c) obtained by considering the atoms forming the core of the ribbon (green region in the atomistic model of Figure 6, right). By choice, the core consists of those atoms that are separated by at least 4 Å from the surfaces. Upon core projection, not only does peak 1 disappear, but we found a sizable decrease of the DOS at the top of the valence band (peak 2) so that the projected DOS is more similar (though not identical) to the bulk. This trend is further confirmed by larger ribbons for which the fraction of atoms of the core is higher. It is demonstrated in this way that feature 2 is associated with the outer region of the NWs.

Passivation of the Nanowires by Organic Ligands. It is important to identify effective ways to get rid of the surface states described above by a proper saturation of the missing electronic interactions. Colloidal synthesis of Bi_2S_3 typically makes use of organic ligands such as oleic acid or oleylamine^{31,39} with carboxylic (COOH) and amine anchoring groups (NH_2), respectively. These ligands consist of a polar head that attaches to the nanocrystal surface and a long hydrophobic aliphatic chain that acts as a shell for the nanoparticle. Amine molecules have been used in the synthesis of NWs reported by Cademartiri et al.^{39,40} The same molecules have also been adopted in the synthesis of the present work, though with a different bismuth precursor. In contrast, carboxylic groups have been used in other studies for the synthesis of nanorods at temperatures >50 °C.³¹ Despite experiments⁴⁹ showing that a complete capping of the NWs is possible, the absence of photoluminescence in the colloidal syntheses suggests that at least a small fraction of the surface sites are not passivated. The purpose of the following investigation is to clarify the effect of the different ligands on different atomic sites of the surface. We focus on acetic acid (CH_3COOH) and methylamine (CH_3NH_2), small molecules that have the same anchoring group of oleic acid or oleylamine, respectively, but with the shortest possible aliphatic tail in order to minimize the steric repulsion between molecules. Having observed (in the previous subsection) that the intragap states are related to the sulfurs atoms at the edges of the NWs, our first attempt consists of the full coverage of edge sites by the organic molecules, i.e., one molecule per sulfur atom of the edge. The results show that both arrays of molecules bind to the edges of the NWs (Figure 7). In the case of acetic acid (Figure 7b), the hydrogen of the carboxylic group binds to the unsaturated sulfurs of the NW, whereas the other oxygen of the molecule is oriented toward the nearest bismuth. With the methylamine molecule, the nitrogen binds to the bismuth atom that is connected with the unsaturated sulfur (Figure 7c). The adhesion energy of the acetic acid on the NWs is 0.7 eV per molecule. The methylamine molecule has a lower adhesion of 0.4 eV per molecule. According to our simulations, acetic acid does not deprotonate spontaneously in binding with Bi_2S_3 NWs. Similar calculations performed by starting from deprotonated configurations (COO^-) give rise to smaller binding energies.

The ability of ligands to restore a clean gap is shown in Figure 7 (top panels), which reported the band structure of the 4-ribbon NW before (Figure 7a) and after the saturation with CH_3COOH (Figure 7b) or CH_3NH_2 (Figure 7c). It can be observed that the saturation by acetic acid lowers the surface level below the valence band, thus restoring a clean gap. In the case of methylamine, the lowering is less efficient, and the defect level still remains above the valence band at Γ . Hence, the acetic acid seems to be more efficient than methylamine

molecules in the removal of surface states from the band gap of the Bi_2S_3 NWs. However, in both cases the molecules widen the gap up to 1.5 and 1.4 eV for acetic acid and methylamine, respectively. It is interesting to note that molecular passivation does not affect the valence bands of the NWs, which is practically unchanged with respect to the free NW. This confirms that the augmented DOS at the top of the valence band of the NW with respect to the bulk (discussed above as feature 2 of Figure 6) is not related to the electronic defects at the edges but rather to surface strain on the other atomic sites of the surface. We performed further simulations by binding the ligands to the sulfur and bismuth atoms of the NW surface at sites different from the edges (Figure S2, Supporting Information). The binding energies are very close to those obtained saturating the edge sites. However, the intragap states are not eliminated by the molecules, confirming the critical role of edges as source of electronic defects. Nevertheless, this kind of coverage is beneficial from a structural point of view because the system partly recovers its bulk arrangement. This is in agreement with the experimental observation that the crystalline geometry of the fully covered NW is indistinguishable from the bulk structure.⁴⁹

Sulfur Vacancies in the Nanowires. Because the edge levels of the ribbons are associated with the outer sulfur atoms of the NWs, it is interesting to understand the effect of the removal of such atoms. This is equivalent to considering the presence of sulfur vacancies at the NW surfaces. Actually, these kinds of point defects are known to be the most abundant in bismuth sulfide.⁴⁷ We performed simulations on the 4-ribbon NW by removing all the sulfur atoms at the ribbon edges and fully relaxing the atomic positions. The final NW structure is depicted in Figure 8. The sulfur vacancies give rise to two

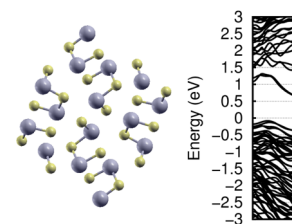


Figure 8. Left: 4-ribbon nanowire containing two sulfur vacancies (edge atoms removed). Right: corresponding band structure.

doubly occupied levels deeply located within the band gap. We conclude that sulfur vacancies are not able to compensate for the surface states but instead generate doubly occupied deep states located 0.5 eV below the conduction band. Accordingly, we expect to detect trap states in Bi_2S_3 samples containing sulfur vacancies, which is in fact observed by spectroscopic measurements.³¹

Conclusions. The structure, stability, and electronic properties of Bi_2S_3 nanowires are studied by ab initio simulations and experiments. We demonstrate that crystalline ultrathin nanowires are expected to be energetically stable at room temperature. TEM analysis reveals nanostructures with diameters down to 3 nm that extend for 300 nm along the [010] crystallographic direction with a coherence length of about 30 nm. Electronic properties are further investigated theoretically. The surface of the nanowire induces intragap doubly occupied states 300 meV above the valence band and associated with the sulfur atoms of the NWs edges. Because of the peculiar crystalline structure of Bi_2S_3 , such defects can be

described as 1D-like surface states extending along the nanowires axes. The removal of the edge sulfur atoms is not beneficial for the system because the surface vacancies give rise to doubly occupied intragap states located around 250 meV below the conduction band minimum.

Intragap states can be instead eliminated by passivating the surfaces of the nanowires with carboxylic and amine groups. Calculations show that both groups are able to eliminate the surface states and in particular small molecules, such as acetic acid and methylamine, can fully passivate all the defective sites at the NW surfaces. This suggests a possible route for improving the optoelectronic properties of Bi₂S₃ nanostructures by tuning the ligand size.

METHODS

Computational Methods. We performed DFT calculations by the QUANTUM ESPRESSO code.⁵² The initial geometry was chosen corresponding to the experimental data reported by Lundegaard et al.⁵³ We used the Perdew–Burke–Ernzerhof (PBE)⁵⁴ functional within the generalized gradient approximation (GGA) of DFT to perform geometry optimizations. The valence-electron wave functions are expanded in plane waves basis sets with kinetic energy cutoff of 30 Ry. Valence electrons are explicitly described, whereas the core–valence interaction is taken into account by means of Troullier–Martins pseudopotentials⁵⁵ generated using the fhi98 code.⁵⁶ The reciprocal space was sampled with a $1 \times 4 \times 1$ Brillouin zone mesh centered at Γ , according to the single-dimensionality of the nanowires. Both the energy cutoff and the number of k-points were tested to be sufficient to ensure convergence of the total energy of the system.

Experimental Methods. We synthesized the Bi₂S₃ nanowires with an oleylamine-based procedure. All reagents were obtained from Sigma-Aldrich and were used as received. A mixture of bismuth acetate (3.2 mmol) and oleylamine (OAm, 4.2 mL) was stirred and heated to 130 °C over the course of 30 min and then kept at the same temperature for 30 min under Ar atmosphere. A solution of 15.3 mmol of sulfur dissolved in 10 mL of OAm was quickly injected into the flask. After 30 min at 100 °C, the reaction was quenched with cold toluene. Unsolubilized materials were removed by centrifugation. Then, acetone was added to the supernatant until it became turbid, and the mixture was centrifuged, the supernatant discarded, and the precipitated nanocrystals redispersed in toluene. For the TEM observations, the stable Bi₂S₃–toluene dispersions are directly dropped on carbon-coated copper grids. TEM and HRTEM images were obtained with a JEOL 2010 UHR equipped with a Gatan imaging filter (GIF) with a 15 eV window and a 794 slow-scan CCD camera.

ASSOCIATED CONTENT

Supporting Information

Further experimental procedures and details about the atomistic methods. The Supporting Information is available free of charge on the ACS Publications website at DOI: 10.1021/acs.jpcc.5b02702.

AUTHOR INFORMATION

Corresponding Author

*Phone: +390706754868. E-mail: mattoni@iom.cnr.it.

Notes

The authors declare no competing financial interest.

ACKNOWLEDGMENTS

We acknowledge financial support by Regione Autonoma della Sardegna under L. R. 7/2007 (CRP-24978 and CRP-18013), by CompuNet, Istituto Italiano di Tecnologia, and computational support by CINECA (Casalecchio di Reno, Italy), through ISCRA Projects DEPA-BIS and CRS4 (Loc. Piscina Manna, Pula, Italy).

REFERENCES

- (1) Colvin, V. L.; Schlamp, M. C.; Alivisatos, A. P. Light-emitting diodes made from cadmium selenide nanocrystals and a semiconducting polymer. *Nature* **1994**, *370*, 354–357.
- (2) Schlamp, M. C.; Peng, X. G.; Alivisatos, A. P. Improved efficiencies in light emitting diodes made with CdSe(CdS) core/shell type nanocrystals and a semiconducting polymer. *J. Appl. Phys.* **1997**, *82*, 5837–5842.
- (3) Sun, Q.; et al. Bright, multicoloured light-emitting diodes based on quantum dots. *Nat. Photonics* **2007**, *1*, 717–722.
- (4) Konstantatos, G.; Howard, L.; Fischer, A.; Hoogland, S.; Clifford, J.; Klem, E.; Levina, L.; Sargent, E. H. Ultrasensitive solution-cast quantum dot photodetectors. *Nature* **2006**, *442*, 180–183.
- (5) Konstantatos, G.; Levina, L.; Tang, J.; Sargent, E. H. Sensitive solution-processed Bi₂S₃ nanocrystalline photodetectors. *Nano Lett.* **2008**, *8*, 4002–4006.
- (6) Huynh, W. U.; Dittmer, J. J.; Alivisatos, A. P. Hybrid nanorod-polymer solar cells. *Science* **2002**, *295*, 2425–2427.
- (7) Huynh, W. U.; Dittmer, J. J.; Libby, W. C.; Whiting, G. L.; Alivisatos, A. P. Controlling the morphology of nanocrystal-polymer composites for solar cells. *Adv. Funct. Mater.* **2003**, *13*, 73–79.
- (8) Gunes, S.; Neugebauer, H.; Sariciftci, N. S.; Roither, K. M.; Kovalenko, M.; Pillwein, H.; Heiss, G. W. Hybrid solar cells using HgTe nanocrystals and nanoporous TiO₂ electrodes. *Adv. Funct. Mater.* **2006**, *16*, 1095–1099.
- (9) Lee, J. S.; Shevchenko, E. V.; Talapin, D. V. Au-PbS core-shell nanocrystals: plasmonic absorption enhancement and electrical doping via intra-particle charge transfer. *J. Am. Chem. Soc.* **2008**, *130*, 9673–9675.
- (10) Kim, D. W.; Jang, J.; Kim, H.; Cho, K.; Kim, S. Electrical characteristics of HgTe nanocrystal-based thin film transistors fabricated on flexible plastic substrates. *Thin Solid Films* **2008**, *516*, 7715–7719.
- (11) Nair, P.; Nair, M.; Garcia, V.; Arenas, O.; Pea, Y.; Castillo, A.; Ayala, I.; Gomezdaza, O.; Sanchez, A.; Campos, J.; et al. Semiconductor thin films by chemical bath deposition for solar energy related applications. *Sol. Energy Mater. Sol. Cells* **1998**, *52*, 313–344.
- (12) Walton, R. I. Subcritical solvothermal synthesis of condensed inorganic materials. *Chem. Soc. Rev.* **2002**, *31*, 230–238.
- (13) Yin, Y.; Alivisatos, A. P. Colloidal nanocrystal synthesis and the organic-inorganic interface. *Nature* **2005**, *437*, 664–670.
- (14) Tahir, A. A.; Ehsan, M. A.; Mazhar, M.; Wijayantha, K. G. U.; Zeller, M.; Hunter, A. D. Photoelectrochemical and photoresponsive properties of Bi₂S₃ nanotube and nanoparticle thin films. *Chem. Mater.* **2010**, *22*, 5084–5092.
- (15) Calzia, V.; Mallocci, G.; Bongiovanni, G.; Mattoni, A. Electronic properties and quantum confinement in Bi₂S₃ ribbon-like nanostructures. *J. Phys. Chem. C* **2013**, *117*, 21923–21929.
- (16) Sharma, Y.; Srivastava, P.; Dashora, A.; Vadkhiya, L.; Bhayani, M.; Jain, R.; Jani, A.; Ahuja, B. Electronic structure, optical properties and Compton profiles of Bi₂S₃ and Bi₂Se₃. *Solid State Sci.* **2012**, *14*, 241–249.
- (17) Filip, M. R.; Patrick, C. E.; Giustino, F. GW quasiparticle band structures of stibnite, antimonelite, bismuthinite, and guanajuatite. *Phys. Rev. B: Condens. Matter Mater. Phys.* **2013**, *87*, 205125.
- (18) Koc, H.; Ozisik, H.; Deligöz, E.; Mamedov, A. M.; Ozbay, E. Mechanical, electronic, and optical properties of Bi₂S₃ and Bi₂Se₃ compounds: first principle investigations. *J. Mol. Model.* **2014**, *20*, 2180.

- (19) Yesugade, N.; Lokhande, C.; Bhosale, C. Structural and optical properties of electrodeposited Bi₂S₃, Sb₂S₃ and As₂S₃ thin films. *Thin Solid Films* **1995**, *263*, 145–149.
- (20) Lukose, J.; Pradeep, B. Electrical and optical properties of bismuth sulphide [Bi₂S₃] thin films prepared by reactive evaporation. *Solid State Commun.* **1991**, *78*, 535–538.
- (21) Mahmoud, S.; Eid, A. H.; Omar, H. Optical characteristics of bismuth sulfide (Bi₂S₃) thin films. *Fizika A* **1997**, *6*, 111–120.
- (22) Konstantatos, G.; Levina, L.; Tang, J.; Sargent, E. H. Sensitive solution-processed Bi₂S₃ nanocrystalline photodetectors. *Nano Lett.* **2008**, *8*, 4002–4006.
- (23) Rath, A. K.; Bernechea, M.; Martinez, L.; Konstantatos, G. Solution-processed heterojunction solar cells based on p-type PbS quantum dots and n-type Bi₂S₃ nanocrystals. *Adv. Mater.* **2011**, *23*, 3712–3717.
- (24) Rath, A. K.; Bernechea, M.; Martinez, L.; de Arquer, F. P. G.; Osmond, J.; Konstantatos, G. Solution-processed inorganic bulk nano-heterojunctions and their application to solar cells. *Nat. Photonics* **2012**, *6*, 529–534.
- (25) Martinez, L.; Bernechea, M.; de Arquer, F. P. G.; Konstantatos, G. Near IR-sensitive, non-toxic, polymer/nanocrystal solar cells employing Bi₂S₃ as the electron acceptor. *Adv. Energy Mater.* **2011**, *1*, 1029–1035.
- (26) Martinez, L.; Higuchi, S.; MacLachlan, A. J.; Stavrinadis, A.; Miller, N. C.; Diedenhofen, S. L.; Bernechea, M.; Sweetnam, S.; Nelson, J.; Haque, S. A.; et al. Improved electronic coupling in hybrid organic-inorganic nanocomposites employing thiol-functionalized P3HT and bismuth sulfide nanocrystals. *Nanoscale* **2014**, *6*, 10018–10026.
- (27) Yu, H.; Bao, H.; Zhao, K.; Du, Z.; Zhang, H.; Zhong, X. Topotactically grown bismuth sulfide network film on substrate as low-cost counter electrodes for quantum dot-sensitized solar cells. *J. Phys. Chem. C* **2014**, *118*, 16602–16610.
- (28) Kinsella, J. M.; Jimenez, R. E.; Karmali, P. P.; Rush, A. M.; Kotamraju, V. R.; Gianneschi, N. C.; Ruoslahti, E.; Stupack, D.; Sailor, M. J. X-ray computed tomography imaging of breast cancer by using targeted peptide-labeled bismuth sulfide nanoparticles. *Angew. Chem., Int. Ed.* **2011**, *50*, 12308–12311.
- (29) Liu, J.; Zheng, X.; Yan, L.; Zhou, L.; Tian, G.; Yin, W.; Wang, L.; Liu, Y.; Hu, Z.; Gu, Z.; et al. Bismuth sulfide nanorods as a precision nanomedicine for in vivo multimodal imaging-guided photothermal therapy of tumor. *ACS Nano* **2015**, *9*, 696–707.
- (30) Chen, J.; Yang, X.-Q.; Meng, Y.-Z.; Huang, H.-H.; Qin, M.-Y.; Yan, D.-M.; Zhao, Y.-D.; Ma, Z.-Y. In vitro and in vivo CT imaging using bismuth sulfide modified with a highly biocompatible Pluronic F127. *Nanotechnology* **2014**, *25*, 295103.
- (31) Aresti, M.; Saba, M.; Piras, R.; Marongiu, D.; Mula, G.; Quochi, F.; Mura, A.; Cannas, C.; Mureddu, M.; Ardu, A.; et al. Colloidal Bi₂S₃ nanocrystals: quantum size effects and midgap states. *Adv. Funct. Mater.* **2014**, *24*, 3341–3350.
- (32) Peter, L. M.; Wijayantha, K. G. U.; Riley, D. J.; Waggett, J. P. Band-edge tuning in self-assembled layers of Bi₂S₃ nanoparticles used to photosensitize nanocrystalline TiO₂. *J. Phys. Chem. B* **2003**, *107*, 8378–8381.
- (33) Stavila, V.; Whitmire, K. H.; Rusakova, I. Synthesis of Bi₂S₃ nanostructures from bismuth(III) thiourea and thiosemicarbazide complexes. *Chem. Mater.* **2009**, *21*, 5456–5465.
- (34) Zhu, X.; Ma, J.; Wang, Y.; Tao, J.; Lin, B.; Ren, Y.; Jiang, X.; Liu, J. Morphology-controlled synthesis and characterization of bismuth sulfide crystallites via a hydrothermal method. *Ceram. Int.* **2008**, *34*, 249–251.
- (35) Quan, Z.; Yang, J.; Yang, P.; Wang, Z.; Li, C.; Lin, J. Facile synthesis and characterization of single crystalline Bi₂S₃ with various morphologies. *Cryst. Growth Des.* **2008**, *8*, 200–207.
- (36) Liao, H.-C.; Wu, M.-C.; Jao, M.-H.; Chuang, C.-M.; Chen, Y.-F.; Su, W.-F. Synthesis, optical and photovoltaic properties of bismuth sulfide nanorods. *CrystEngComm* **2012**, *14*, 3645–3652.
- (37) Kawade, U. V.; Panmand, R. P.; Sethi, Y. A.; Kulkarni, M. V.; Apte, S. K.; Naik, S. D.; Kale, B. B. Environmentally benign enhanced hydrogen production via lethal H₂S under natural sunlight using hierarchical nanostructured bismuth sulfide. *RSC Adv.* **2014**, *4*, 49295–49302.
- (38) Xue, B.; Sun, T.; Mao, F.; Xie, J. Gelatin-assisted green synthesis of bismuth sulfide nanorods under microwave irradiation. *Mater. Lett.* **2014**, *122*, 106–109.
- (39) Cademartiri, L.; Malakooti, R.; O'Brien, P. G.; Migliori, A.; Petrov, S.; Kherani, N. P.; Ozin, G. A. Large-scale synthesis of ultrathin Bi₂S₃ necklace nanowires. *Angew. Chem., Int. Ed.* **2008**, *47*, 3814–3817.
- (40) Cademartiri, L.; Scotognella, F.; O'Brien, P. G.; Lotsch, B. V.; Thomson, J.; Petrov, S.; Kherani, N. P.; Ozin, G. A. Cross-linking Bi₂S₃ ultrathin nanowires: a platform for nanostructure formation and biomolecule detection. *Nano Lett.* **2009**, *9*, 1482–1486.
- (41) Yu, Y.; Jin, C. H.; Wang, R. H.; Chen, Q.; Peng, L.-M. High-quality ultralong Bi₂S₃ nanowires: structure, growth, and properties. *J. Phys. Chem. B* **2005**, *109*, 18772–18776.
- (42) Bao, H.; Cui, X.; Li, C. M.; Gan, Y.; Zhang, J.; Guo, J. Photoswitchable semiconductor bismuth sulfide (Bi₂S₃) nanowires and their self-supported nanowire arrays. *J. Phys. Chem. C* **2007**, *111*, 12279–12283.
- (43) Chen, Z.; Cao, M. Synthesis, characterization, and hydrophobic properties of Bi₂S₃ hierarchical nanostructures. *Mater. Res. Bull.* **2011**, *46*, 555–562.
- (44) Jiang, J.; Yu, S.-H.; Yao, W.-T.; Ge, H.; Zhang, G.-Z. Morphogenesis and crystallization of Bi₂S₃ nanostructures by an ionic liquid-assisted templating route: synthesis, formation mechanism, and properties. *Chem. Mater.* **2005**, *17*, 6094–6100.
- (45) Xu, Y.; Ren, Z.; Cao, G.; Ren, W.; Deng, K.; Zhong, Y. A template-free route to prepare Bi₂S₃ nanostructures. *Phys. B* **2010**, *405*, 1353–1358.
- (46) Tang, C.; Su, J.; Hu, Q.; Yang, Y.; Wang, C.; Zhao, C.; Zang, C.; Zhang, Y. Facile synthesis of Bi₂S₃ network nanostructure. *Solid State Sci.* **2011**, *13*, 1152–1156.
- (47) Zhan, S.-Q.; Wan, H.; Xu, L.; Huang, W.-Q.; Huang, G.-F.; Long, J.-P.; Peng, P. Native vacancy defects in bismuth sulfide. *Int. J. Mod. Phys. B* **2014**, *28*, 1450150.
- (48) Tang, J.; Alivisatos, A. P. Crystal splitting in the growth of Bi₂S₃. *Nano Lett.* **2006**, *6*, 2701–2706.
- (49) Thomson, J. W.; Cademartiri, L.; MacDonald, M.; Petrov, S.; Calestani, G.; Zhang, P.; Ozin, G. A. Ultrathin Bi₂S₃ nanowires: surface and core structure at the cluster-nanocrystal transition. *J. Am. Chem. Soc.* **2010**, *132*, 9058–9068.
- (50) Patrick, C. E.; Giustino, F. Structural and electronic properties of semiconductor-sensitized solar-cell interfaces. *Adv. Funct. Mater.* **2011**, *21*, 4663–4667.
- (51) Larson, P.; Greanya, V. A.; Tonjes, W. C.; Liu, R.; Mahanti, S. D.; Olson, C. G. Electronic structure of Bi₂X₃ (X = S, Se, Te) compounds: comparison of theoretical calculations with photoemission studies. *Phys. Rev. B: Condens. Matter Mater. Phys.* **2002**, *65*, 085108.
- (52) Giannozzi, P.; Baroni, S.; Bonini, N.; Calandra, M.; Car, R.; Cavazzoni, C.; Ceresoli, D.; Chiarotti, G. L.; Cococcioni, M.; Dabo, I.; et al. QUANTUM ESPRESSO: a modular and open-source software project for quantum simulations of materials. *J. Phys.: Condens. Matter* **2009**, *21*, 395502–395521.
- (53) Lundegaard, L.; Makovicky, E.; Boffa-Ballaran, T.; Balic-Zunic, T. Crystal structure and cation lone electron pair activity of Bi₂S₃ between 0 and 10 GPa. *Phys. Chem. Miner.* **2005**, *32*, 578–584.
- (54) Perdew, J. P.; Burke, K.; Ernzerhof, M. Generalized gradient approximation made simple. *Phys. Rev. Lett.* **1996**, *77*, 3865–3868.
- (55) Troullier, N.; Martins, J. L. Efficient pseudopotentials for plane-wave calculations. *Phys. Rev. B: Condens. Matter Mater. Phys.* **1991**, *43*, 1993–2006.
- (56) Fuchs, M.; Scheffler, M. Ab initio pseudopotentials for electronic structure calculations of poly-atomic systems using density-functional theory. *Comput. Phys. Commun.* **1999**, *119*, 67–98.